



Cite this: *RSC Adv.*, 2018, 8, 35187

Preparation, characterization, and luminescence properties of double perovskite $\text{SrLaMgSbO}_6\text{:Mn}^{4+}$ far-red emitting phosphors for indoor plant growth lighting

Liangling Sun, Jia Liang, Balaji Devakumar, Qi Sun, Shaoying Wang, Bin Li and Xiaoyong Huang *

Mn^{4+} -activated SrLaMgSbO_6 far-red emitting phosphors with double perovskite structure were prepared by traditional solid-state reaction. The research on the crystal structure of the $\text{SrLaMgSbO}_6\text{:0.8\%Mn}^{4+}$ (SLMS:0.8%Mn⁴⁺) phosphors showed that the as-prepared sample was made up of two polyhedrons, $[\text{SbO}_6]$ and $[\text{MgO}_6]$. Under the excitation of 333 nm, the SLMS:0.8%Mn⁴⁺ phosphors exhibited an intense far-red emission in the 625–800 nm wavelength range with CIE chromaticity coordinates of (0.733, 0.268), which could match well with the absorption spectrum of phytochrome P_{FR} . The optimal concentration of Mn^{4+} ions in the SLMS:Mn⁴⁺ phosphors was 0.8 mol%. Importantly, the as-prepared SLMS:0.8%Mn⁴⁺ phosphors had an internal quantum efficiency of 35%. The thermal stability of SLMS:0.8%Mn⁴⁺ phosphors was also investigated, and the activation energy was found to be 0.3 eV. Thus, the Mn^{4+} -activated SLMS phosphors have great potential to serve as far-red emitting phosphors in indoor plant growth lighting.

Received 21st August 2018
Accepted 8th October 2018

DOI: 10.1039/c8ra06983b

rsc.li/rsc-advances

Introduction

Nowadays, an intense research effort has recently been devoted to developing red-emitting phosphors for phosphor-converted light-emitting diodes (pc-LEDs), due to the fact that pc-LEDs, which show many merits including high durability, low energy consumption, short response time, and environmental protection, can be used in indoor plant cultivation, decoration, and medical applications.^{1–9} For the indoor plant growth, the growth status can be controlled by adjusting the ratio of the phytochrome P_{R} and P_{FR} , because the P_{FR} can convert to P_{R} by absorbing far-red light centered at 730 nm.^{10,11} But in the agricultural industry, especially indoor plant cultivation, there is lack of far-red light to meet the requirement of mutual transformation between the phytochrome P_{FR} and P_{R} due to small percentage of far-red light in the sunlight compared to red light.^{10,12} Meanwhile, the traditional lamp cannot match well with the absorption spectrum of the phytochrome P_{FR} . So pc-LEDs play an important role in indoor plant growth, and many research on the phosphors used in indoor plant growth lighting have been implemented such as $\text{Ca}_{1-x}\text{Y}_x\text{Al}_{12-x}\text{Mg}_x\text{O}_{19}\text{:Mn}^{4+}$,¹³ $\text{La}(\text{MgTi})_{1/2}\text{O}_3\text{:Mn}^{4+}$,¹⁰ $\text{Ca}_{14}\text{Al}_{10}\text{Zn}_6\text{O}_{35}\text{:Bi}^{3+},\text{Mn}^{4+}$,¹⁴ $\text{SrMg}_2\text{-La}_2\text{W}_2\text{O}_{12}\text{:Mn}^{4+}$,¹⁵ and $\text{Ca}_3\text{Al}_4\text{ZnO}_{10}\text{:Bi}^{3+},\text{Mn}^{4+}$.¹⁶ Since the

far-red emitting phosphors are vital to the pc-LEDs and relatively little research has been conducted on that kind of phosphors, thus it is meaningful to study the far-red emitting phosphors for applications in indoor plant cultivation.

It is known that Mn^{4+} ions with a $3d^3$ electronic configuration in a strong crystal fields of octahedral coordination (coordination number (CN) = 6) can give rise to red emission in the wavelength region of 620–800 nm owing to the spin-forbidden $^2\text{E}_g \rightarrow ^4\text{A}_{2g}$ transition.^{17–24} Mn^{4+} -doped phosphors contain two categories: (1) Mn^{4+} -activated fluorides, such as $\text{Li}_3\text{Na}_3\text{Ga}_2\text{F}_{12}\text{:Mn}^{4+}$ ($\lambda_{\text{em}} = 627$ nm),²⁵ $\text{Na}_3\text{TaF}_8\text{:Mn}^{4+}$ ($\lambda_{\text{em}} = 627$ nm),²⁶ and $\text{K}_3\text{ScF}_6\text{:Mn}^{4+}$ ($\lambda_{\text{em}} = 631$ nm);²⁷ and (2) Mn^{4+} -activated oxides, such as $\text{Ca}_3\text{La}_2\text{W}_2\text{O}_{12}\text{:Mn}^{4+}$ ($\lambda_{\text{em}} = 711$ nm),²⁸ $\text{Li}_2\text{MgZrO}_4\text{:Mn}^{4+}$ ($\lambda_{\text{em}} = 670$ nm),²⁹ and $\text{Ba}_2\text{GdSbO}_6\text{:Mn}^{4+}$ ($\lambda_{\text{em}} = 687$ nm).³⁰ Mn^{4+} -activated fluorides generally exhibit red emissions in the 600–650 nm wavelength range and they are widely used in white LEDs application.^{13,30–33} In sharp contrast, Mn^{4+} -activated oxides showed far-red emissions at around 700 nm, which are vital to plant growth in photomorphogenesis process. So Mn^{4+} -activated oxides have potential applications as spectral converters for pc-LEDs towards indoor plant growth lighting.^{14,34,35}

In recent years, double-perovskite oxides with octahedral crystal sites are considered as good host materials for Mn^{4+} activator.^{35–37} In a previous paper by Liu and co-workers, the $\text{Sr}_{1-x}\text{Ca}_x\text{LaMgSbO}_6\text{:Eu}^{3+}$ phosphors have been researched, and the structural analysis shows that the host compound has two kind of octahedral structures, $[\text{MgO}_6]$ and $[\text{SbO}_6]$.³⁸ Thus, in this

College of Physics and Optoelectronics, Taiyuan University of Technology, Taiyuan 030024, P. R. China. E-mail: huangxy04@126.com



present paper, Mn^{4+} -doped SrLaMgSbO_6 (SLMS) phosphors have been synthesized and their crystal structure and optical properties were studied. The SLMS host contains two octahedral structures of $[\text{MgO}_6]$ and $[\text{SbO}_6]$, and the Mn^{4+} ions prefer to occupy the Sb^{5+} sites to form the phase of SLMS:Mn^{4+} . Under the excitation of 333 nm, the SLMS:Mn^{4+} phosphors emitted far-red light peaking at 705 nm in the spectral range from 625 to 800 nm, which was attributed to the ${}^2\text{E}_g \rightarrow {}^4\text{A}_{2g}$ transition of Mn^{4+} ions. More importantly, the emission spectrum of the SLMS:Mn^{4+} phosphors could match well with the absorption curve of phytochrome P_{FR} , indicating the far-red light from the SLMS:Mn^{4+} phosphors could be efficiently absorbed by phytochrome P_{FR} . The CIE chromaticity coordinates, internal quantum efficiency (IQE), and thermal stability of SLMS:Mn^{4+} phosphors were also investigated in detail. The results demonstrated that the Mn^{4+} -activated SLMS phosphors have much potential to serve as far-red emitting phosphors for indoor plant growth lighting.

Experimental section

$\text{SrLaMgSb}_{1-x}\text{O}_6:\text{xMn}^{4+}$ (abbreviated as: SLMS:xMn^{4+} ; $x = 0.05\text{--}1.2\%$) phosphors were synthesized by a traditional solid-state reaction method. The starting materials of SrCO_3 (analytical reagent, AR), La_2O_3 (99.99%), MgO (AR), Sb_2O_5 (99%), and MnCO_3 (AR), were weighed according to the stoichiometric ratio. Using an agate mortar, the mixed starting materials were ground and then transferred to Al_2O_3 crucible to preheat at 500°C for 3 h in air. After cooling to room temperature, the preheated mixtures were reground again into powders for further calcination at 1500°C for 6 h in air to get the target SLMS:xMn^{4+} phosphors.

The X-ray diffraction (XRD) patterns and morphology properties of SLMS:xMn^{4+} phosphors were measured on a X-ray diffractometer (Cu-K α radiation; Bruker D8 Advance) and a field-emission scanning electron microscope (FE-SEM; MAIA3 TES-CAN), respectively. Structure refinements were made using Fullprof program. The room-temperature photoluminescence (PL) spectra and the PL excitation (PLE) spectra were measured by an Edinburgh FS5 spectrofluorometer with a 150 W continued-wavelength xenon lamp. The luminescence decay lifetimes, the temperature-dependent spectra, and IQE were recorded by using the same spectrofluorometer, equipping with a pulsed xenon lamp, a temperature controller, and an integrating sphere, respectively. The prototype far-red light-emitting device was fabricated by coating the SLMS:0.8\%Mn^{4+} phosphors onto a 365 nm near-UV InGaN LED chip, and the corresponding electroluminescent (EL) properties were measured by using a spectroradiometer system (HAAS-2000, Everfine).

Results and discussion

Fig. 1 shows the XRD patterns of the SLMS:xMn^{4+} ($x = 0.05\%$, 0.8% , and 1.2%) phosphors together with the standard card of the CaLaMgMoO_6 (JCPDS #43-0043). Compared to the standard card of the CaLaMgMoO_6 compound, no other crystalline phase

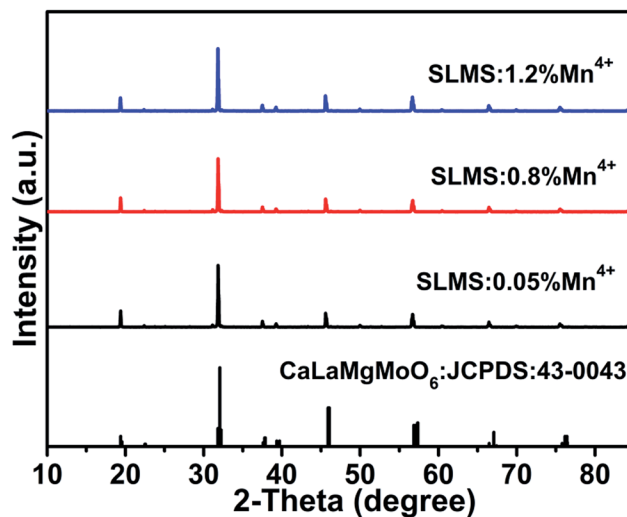


Fig. 1 XRD patterns of the SLMS:xMn^{4+} ($x = 0.05\%$, 0.8% , and 1.2%) phosphors together with the stand card of CaLaMgMoO_6 (JCPDS #43-0043).

was formed in the SLMS:xMn^{4+} phosphors. Fig. 2(a) and Fig. 2(b) represent the refinement result and the corresponding crystal structure of the SLMS:0.8\%Mn^{4+} phosphors, respectively. Table 1 gives the main parameters of the crystal cell for SLMS:0.8\%Mn^{4+} phosphors, in which $a = 5.63586(16) \text{ \AA}$, $b = 5.62543(13) \text{ \AA}$, $c = 7.95407(19) \text{ \AA}$, and $V = 252.177(6) \text{ \AA}^3$. The SLMS:0.8\%Mn^{4+} phosphors with double perovskite structure was belong to monoclinic crystal system and a $P21/n$ space group. The host was composed by two octahedral structures of $[\text{MgO}_6]$ and $[\text{SbO}_6]$. Considering the ion radii and CN of the Sb^{5+} ions ($r = 0.6 \text{ \AA}$, CN = 6), Mg^{2+} ions ($r = 0.72 \text{ \AA}$, CN = 6), and Mn^{4+} ions ($r = 0.53 \text{ \AA}$, CN = 6), the Mn^{4+} ions were more inclined to occupy the Sb^{5+} sites in SLMS host to form the SLMS:Mn^{4+} compound.^{39–41} Another parameter to determine which ions were substituted by Mn^{4+} ions was the radii percentage difference (D_r) between the doping ions (here was Mn^{4+} ions) and the possible substituted ions (here were Sb^{5+} and Mg^{2+} ions). The ratio can be estimated by the following expression:^{42,43}

$$D_r = \frac{R_m(\text{CN}) - R_d(\text{CN})}{R_m(\text{CN})} \times 100\% \quad (1)$$

where $R_m(\text{CN})$ and $R_d(\text{CN})$ are the ionic radii of the host cations (Mg^{2+} and Sb^{5+} ions) and the doped Mn^{4+} ions, respectively. Herein, $R_d(\text{CN}) = 0.53 \text{ \AA}$; the value of $R_m(\text{CN})$ is 0.72 \AA and 0.6 \AA for Mg^{2+} and Sb^{5+} ions, respectively. In this host, CN = 6 for Mn^{4+} , Mg^{2+} , and Sb^{5+} ions. Thus, the values of D_r were 26% and 12% for Mg^{2+} host cation and Sb^{5+} host cation, respectively. Because when Mn^{4+} ions substituted for Mg^{2+} ions, the D_r ratio was higher than Mn^{4+} ions substituted for Sb^{5+} ions, so the Mn^{4+} ions were prefer to substitute for Sb^{5+} than Mg^{2+} ions. On the other hand, the valence of the Sb^{5+} ions was closer to Mn^{4+} ions than Mg^{2+} ions. Therefore, considering the radii and the valence, the Mn^{4+} ions would substitute for Sb^{5+} sites to form the SLMS:Mn^{4+} phosphors. Fig. 3 shows the typical FE-SEM



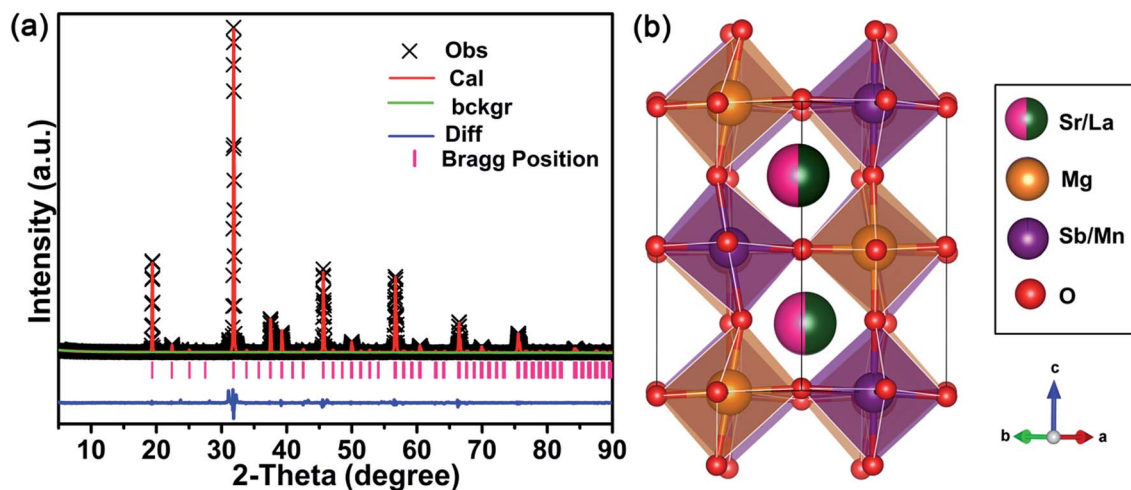


Fig. 2 (a) Rietveld refinement of the XRD pattern for the SLMS:0.8%Mn⁴⁺ phosphors. (b) The crystal structure of the SLMS:0.8%Mn⁴⁺ phosphors.

Table 1 Refined crystallographic parameters of SLMS:0.8%Mn⁴⁺ phosphors

Formula	SLMS:0.8%Mn ⁴⁺
Crystal system	Monoclinic
Space group	<i>P</i> 2 ₁ / <i>n</i>
<i>a</i>	5.63586(16) Å
<i>b</i>	5.62543(13) Å
<i>c</i>	7.95407(19) Å
α	90°
β	90.054(4)°
γ	90°
<i>V</i>	252.177(6) Å ³
<i>R_p</i>	10.53%
<i>R_{wp}</i>	13.86%

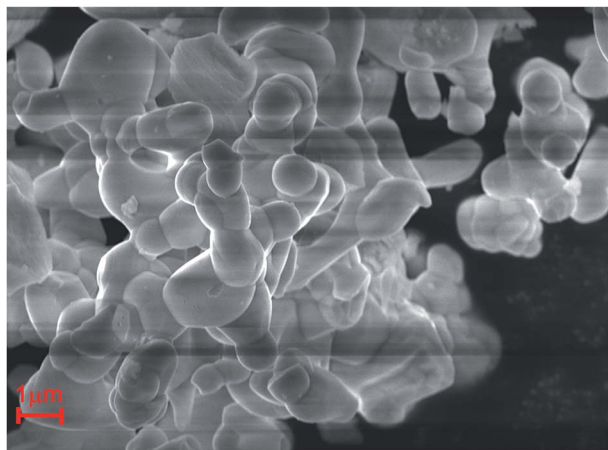


Fig. 3 The typical FE-SEM of SLMS:0.8%Mn⁴⁺ phosphors.

image of the SLMS:0.8%Mn⁴⁺ phosphors. The sizes of the as-prepared sample was found to be about 1–6 μm, and the crystal-surfaces was smooth which was beneficial to get uniform luminescence intensity.

The PLE spectrum ($\lambda_{em} = 705$ nm) of the SLMS:0.8%Mn⁴⁺ phosphors with four Gaussian fitting peaks was shown in Fig. 4(a). Four PLE peaks at 298 nm ($33\,557\text{ cm}^{-1}$; Mn⁴⁺–O^{2–} charge-transfer transition), 338 nm ($29\,586\text{ cm}^{-1}$; $^4A_{2g} \rightarrow ^4T_{1g}$ transition), 423 nm ($23\,641\text{ cm}^{-1}$; $^4A_{2g} \rightarrow ^2T_{2g}$ transition), and 495 nm ($20\,202\text{ cm}^{-1}$; $^4A_{2g} \rightarrow ^4T_{2g}$ transition) were observed, and the PLE peaks at 333 nm and 499 nm dominated the PLE spectrum.^{44–46} Under excitations at 333 nm and 499 nm, the SLMS:0.8%Mn⁴⁺ phosphors exhibited a far-red emission band peaking at 705 nm ($^2E_g \rightarrow ^4A_{2g}$ transition) in the range of 625–800 nm,^{47–49} as shown in Fig. 4(b). Fig. 4(c) displays the PL spectra of the SLMS:*x*Mn⁴⁺ (*x* = 0.05%, 0.6%, 0.8%, 1.0%, and 1.2%) phosphors with different Mn⁴⁺ doping concentrations under 333 nm excitation. As the Mn⁴⁺ concentration increased, the PL intensity firstly showed an increasing trend, and then decreased when the concentration was higher than 0.8 mol%, indicating the occurrence of the concentration quenching effect. Fig. 4(d) shows the luminescence decay curves of the SLMS:*x*Mn⁴⁺ (*x* = 0.05%, 0.6%, 0.8%, 1.0%, and 1.2%) phosphors. The decay lifetimes of the as-prepared samples were obtained by using the following double exponential expression:^{50–53}

$$I = A_1 \exp(-t/\tau_1) + A_2 \exp(-t/\tau_2) \quad (2)$$

herein, *I* refers to the luminescent emission intensity of SLMS:*x*Mn⁴⁺ phosphors at time *t*. τ_1 and τ_2 are the lifetimes for the exponential component; *A*₁ and *A*₂ are constants. Accordingly, the decay lifetimes of the SLMS:*x*Mn⁴⁺ phosphors were found to be 1.257, 1.130, 1.068, 1.034, and 0.950 ms when *x* = 0.05%, 0.6%, 0.8%, 1.0%, and 1.2%, respectively. Obviously, the decay lifetimes decreased with the increasing Mn⁴⁺ concentration, due to the non-radiative energy transfer in the SLMS:Mn⁴⁺ phosphors.⁵⁴

The critical distance (*R*_c) is usually used to determine which kind of interaction contribute to the concentration quenching



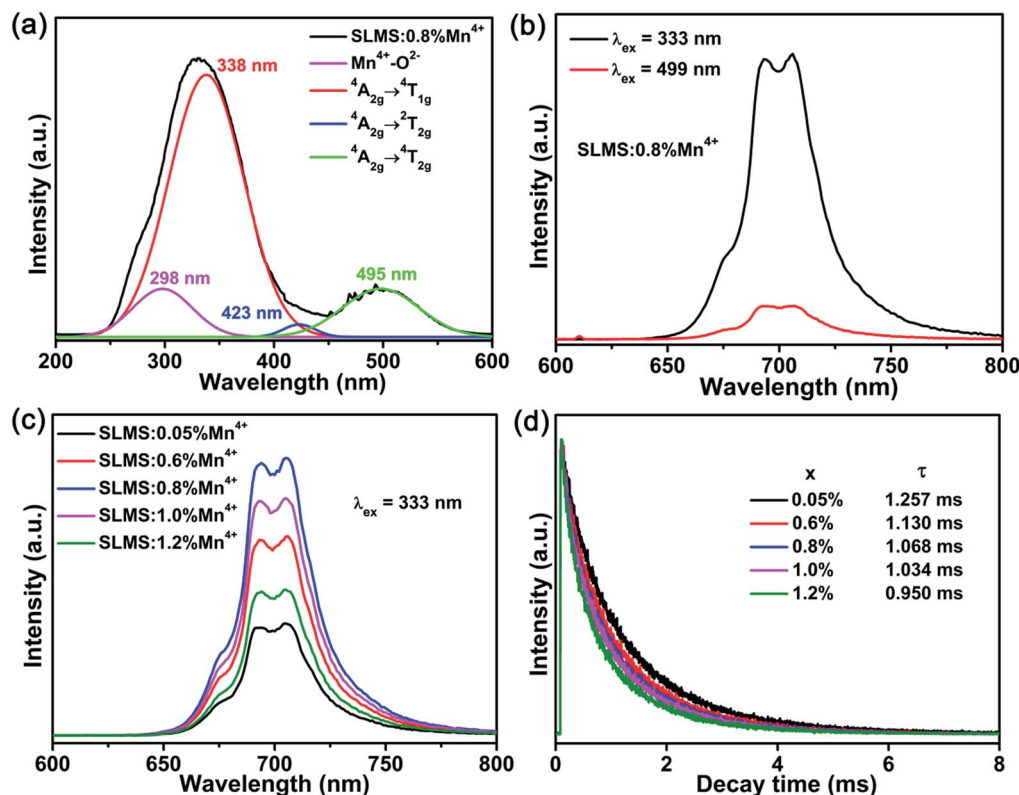


Fig. 4 (a) The PLE spectrum of SLMS:0.8%Mn⁴⁺ phosphors monitored at 705 nm. The four Gaussian fitting curves also displayed in the figure. (b) The PL spectra of SLMS:0.8%Mn⁴⁺ phosphors excited at 333 nm and 499 nm. (c) The PL spectra of SLMS:xMn⁴⁺ (x = 0.05–1.2%) phosphors excited at 333 nm. (d) The luminescence decay curves of SLMS:xMn⁴⁺ (x = 0.05–1.2%) phosphors ($\lambda_{\text{ex}} = 333$ nm; $\lambda_{\text{em}} = 705$ nm).

in phosphors. And the R_c for SLMS:xMn⁴⁺ phosphors can be estimated by the following expression:^{55–58}

$$R_c = 2 \left(\frac{3V}{4\pi x_c N} \right)^{1/3} \quad (3)$$

where V is the volume of the unit cell and x_c is the optimal doping concentration of Mn⁴⁺ ions in SLMS host; N is the number of host cations which is available for Mn⁴⁺ ions to be substituted. In SLMS host, $N = 2$, $V = 252.177(6) \text{ \AA}^3$, and $x_c = 0.8\%$. Thus, the value of x_c was calculated to be 31.1 \AA . The R_c for SLMS:Mn⁴⁺ phosphors was much larger than 5 \AA , and thus the electric multipole interaction was the mechanism responsible for the concentration quenching effect in SLMS:Mn⁴⁺ phosphors.⁵⁹

Fig. 5(a) shows the CIE chromaticity diagram of SLMS:0.8% Mn⁴⁺ phosphors. The corresponding CIE coordinates were determined to be (0.733, 0.268), which were located in the far-red region. Fig. 5(b) compares the PL spectrum of the SLMS:0.8%Mn⁴⁺ phosphors with the absorption spectrum of phytochrome P_{FR} in the range of 500–800 nm, in which the phytochrome P_{FR} was taken from ref. 10. Apparently, the far-red light emission of the SLMS:0.8%Mn⁴⁺ phosphors was matched well with the absorption spectrum of the phytochrome P_{FR}, indicating that the phytochrome P_{FR} was sensitive to the far-red light from the SLMS:0.8%Mn⁴⁺ phosphors. Thus, the luminescent properties of the SLMS:0.8%Mn⁴⁺ phosphors

demonstrated that they had bright prospects to be used in far-red LEDs for indoor plant growth.

The IQE of SLMS:0.8%Mn⁴⁺ phosphors was measured to be 35%, as shown in Fig. 6(a). Moreover, the thermal stability of the SLMS:0.8%Mn⁴⁺ phosphors was also investigated. Fig. 6(b) shows the temperature-dependent PL spectra of the SLMS:0.8% Mn⁴⁺ phosphors under 333 nm excitation. The PL intensity was gradually decreased when the temperature increased, and the emission intensity at 363 K remained about 55% of that at 303 K, which could be seen clearly in Fig. 6(b) and (c). Although the thermal stability was not good as the Ca₂YSbO₆:Mn⁴⁺ (remained 63% at 373 K),⁶⁰ Ca₂LaNbO₆:Mn⁴⁺ (remained about 50% at 400 K),⁴⁰ and CaLaMgNbO₆ (remained about 45% at 423 K),⁴¹ in the next work, we may improve the thermal behavior and luminescence intensity by co-doping another ions such as Li⁺, Na⁺, Mg²⁺, and Ba²⁺.^{49,60–62} Based on the temperature-dependent PL spectra of the SLMS:0.8%Mn⁴⁺ phosphors, the corresponding relationship between $1/kT$ and $\ln(I_0/I - 1)$ was shown in Fig. 6(d), and the activation energy can be estimated by using the following expression:^{38,63,64}

$$I(T) = I_0 \left[1 + c \exp \left(-\frac{\Delta E}{kT} \right) \right]^{-1} \quad (4)$$

where $I(T)$ and I_0 are the PL intensity at temperature T and the initial intensity at 303 K, respectively; c is a constant; k is the Boltzmann constant. The slope was found to be -0.3 , indicating



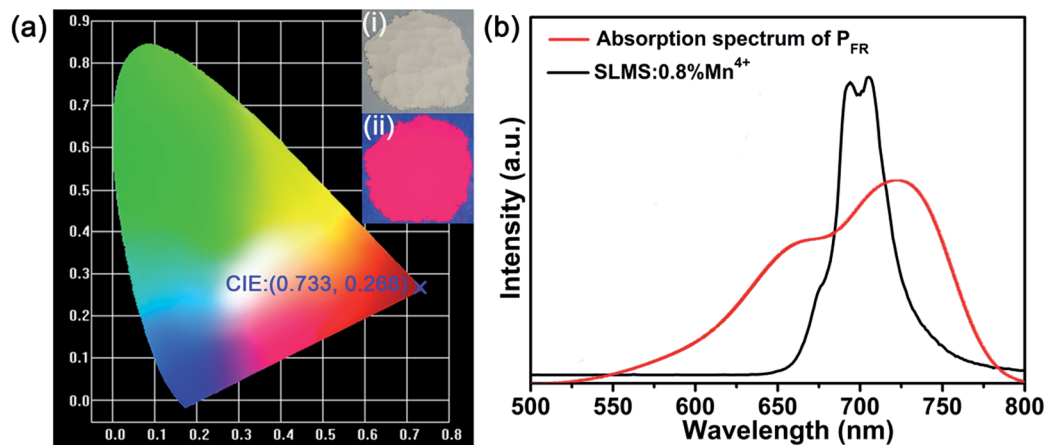


Fig. 5 (a) The CIE chromaticity diagram of the SLMS:0.8%Mn⁴⁺ phosphors. Insets represent the digital photographs under daylight (i) and a 365 nm UV lamp (ii). (b) The PL spectrum of the SLMS:0.8%Mn⁴⁺ phosphors excited at 333 nm and the absorption spectrum of the phytochrome P_{FR}.

the activation energy was 0.3 eV. The possible luminescence thermal quenching process could be expressed by the inset in Fig. 6(d). Generally, under the excitation of 333 nm or 499 nm, the electrons in the ⁴A_{2g} state were firstly excited to the higher ⁴T_{1g} or ⁴T_{2g} level, then relax to the lowest ²E_g excited state by non-radiative process.⁶⁵ After that, the electrons in the ²E_g level

may return to the ground state in two ways. The one way was taken place through ²E_g → ⁴A_{2g} radiation transition (path: 1 → 2) with 705 nm far-red emission, and such process was occurred at room temperature. The other way was that the electrons in the ²E_g level may absorb enough energy to reach the intersection point at higher temperature, then return to the ground state

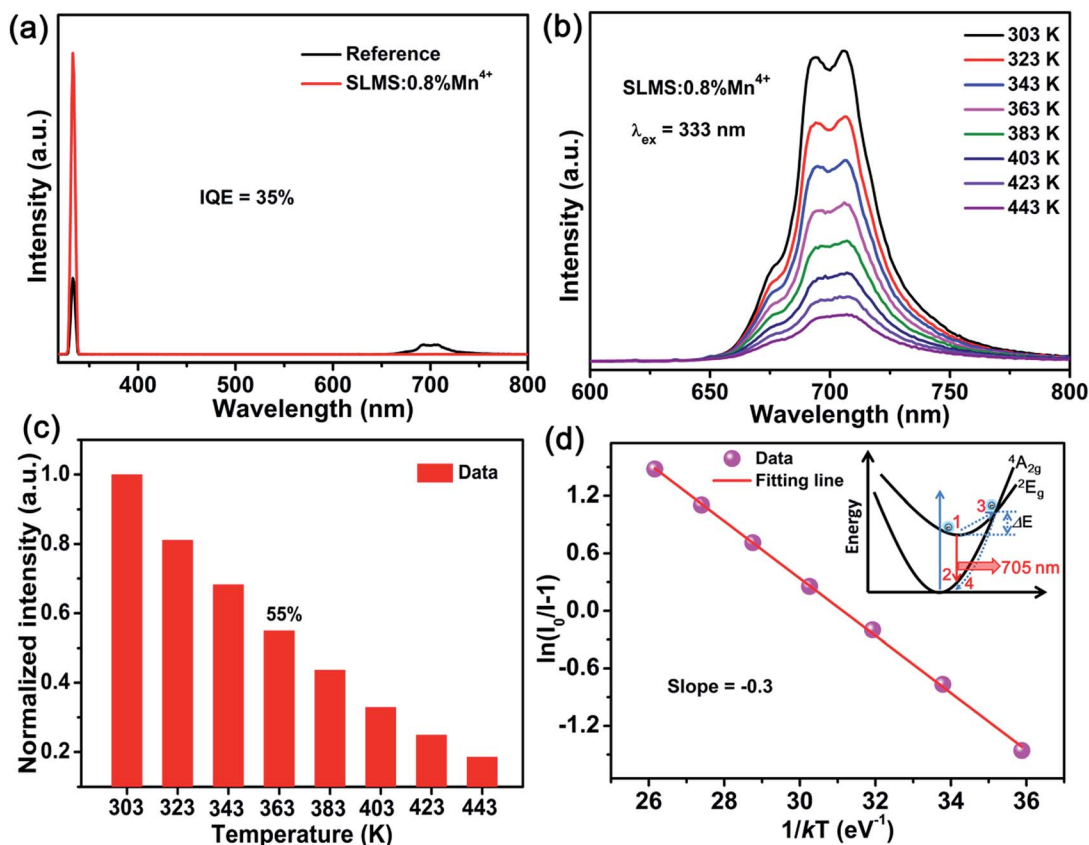


Fig. 6 (a) Excitation profile (λ_{ex} = 333 nm) of the reference BaSO₄ and the emission spectrum of the SLMS:0.8%Mn⁴⁺ phosphors obtained by using an integrating sphere. (b) The temperature-dependent spectra of the SLMS:0.8%Mn⁴⁺ phosphors in the temperature range of 303–443 K. (c) The normalized intensity of the PL intensity as a function of the sample temperature. (d) The plot of 1/kT vs. ln(I₀/I - 1) for the SLMS:0.8%Mn⁴⁺ phosphors. Inset shows the simple configuration coordinate diagram of the ²E_g and ⁴A_{2g} levels of Mn⁴⁺.



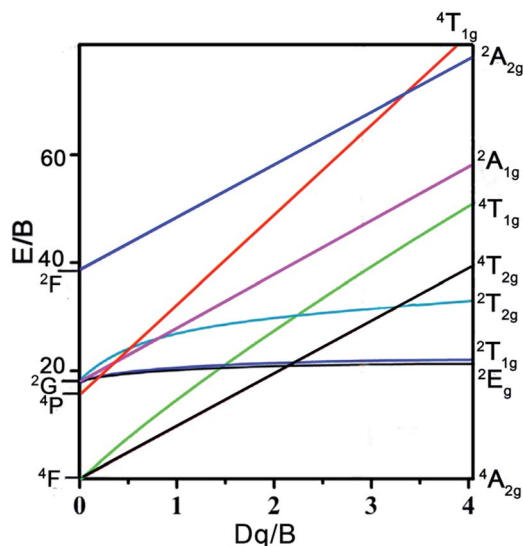


Fig. 7 Tanabe–Sugano energy level diagram of d^3 electron configuration for Mn^{4+} in the octahedral crystal field.

(path: $1 \rightarrow 3 \rightarrow 4$) by non-radiative relaxation and resulted in the decrease of the emission intensity of the SLMS:0.8%Mn $^{4+}$ phosphors.⁶⁶

The crystal-field strength (Dq) and two Racah parameters (B and C) of the SLMS host can be calculated by the following expressions (5)–(8):

$$Dq = E(^4A_{2g} \rightarrow ^4T_{2g})/10 \quad (5)$$

$$\frac{Dq}{B} = \frac{15(x-8)}{(x^2-10x)} \quad (6)$$

$$x = \frac{E(^4A_{2g} \rightarrow ^4T_{1g}) - E(^4A_{2g} \rightarrow ^4T_{2g})}{Dq} \quad (7)$$

$$\frac{E(^2E_g \rightarrow ^4A_{2g})}{B} = \frac{3.05C}{B} + 7.9 - \frac{1.8B}{Dq} \quad (8)$$

where $E(^4A_{2g} \rightarrow ^4T_{1g})$, $E(^4A_{2g} \rightarrow ^4T_{2g})$, and $E(^2E_g \rightarrow ^4A_{2g})$ was obtained from the emission peaks of 338 nm, 495 nm, and 705 nm, respectively. Thus, according to the exp. (5)–(8), the crystal-field strength Dq and Racah parameters B and C were obtained to be 2020, 999, 2356 cm^{-1} , respectively. Correspondingly, the Dq/B was calculated to be 2.02, which was higher than that of the $\text{Lu}_{3-x}\text{Y}_x\text{Al}_5\text{O}_{12}:\text{Mn}^{4+}$ ($Dq/B = 1.45$; $x = 0$),⁴⁹ $\text{Ba}_2\text{YSbO}_6:\text{Mn}^{4+}$ ($Dq/B = 1.88$),⁶¹ and $\text{SrGe}_4\text{O}_9:\text{Mn}^{4+}$ ($Dq/B = 1.20$).⁶⁷ Fig. 7 shows the Tanabe–Sugano energy level diagram of d^3 electron configuration for Mn^{4+} in the octahedral crystal field. Apparently, in an octahedral environment, the ground state $^4A_{2g}$ and excited state $^4T_{1g}$ and $^4T_{2g}$ were split by the 4F term, and the excited state $^2T_{2g}$ and 2E_g were derived from the 2G term.^{39,68} The levels of $^4T_{1g}$, $^4T_{2g}$, $^2T_{2g}$, and 2E_g made up the important energy levels for Mn^{4+} ions to emit far-red light in an octahedral environment.

Fig. 8 shows the EL spectrum of the as-prepared far-red LED device. A far-red emission band in the 600–780 nm wavelength range was observed, attributing to the $^2E_g \rightarrow ^4A_{2g}$ transition.

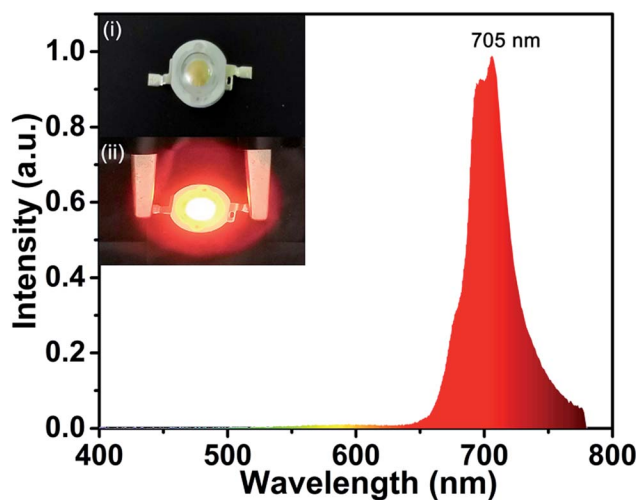


Fig. 8 EL spectrum of the fabricated far-red-emitting LED device by using SLMS:0.8%Mn $^{4+}$ phosphors and a 365 nm near-UV LED chip under a bias current of 240 mA. Insets show the fabricated LED device without (i) and with (ii) a 240 mA bias current.

The external quantum efficiency of the as-prepared far-red LED device was found to be 0.34%. The far-red light from the as-prepared prototype LED device could be easily seen in the inset in Fig. 8. All the results indicated the as-prepared SLMS:Mn $^{4+}$ phosphors have a promising prospect to be used in plant growth LEDs.

Conclusions

In summary, double perovskite SLMS:Mn $^{4+}$ phosphors were synthesized by using the high-temperature solid-state reaction. The excitation band of the SLMS:Mn $^{4+}$ phosphors could be fitted into four Gaussian peaks at 298, 338, 423, and 495 nm. The PL spectrum of the SLMS:Mn $^{4+}$ phosphors showed a far-red emission band peaking at 705 nm, which could match well with the absorption spectrum of the phytochrome P_{FR}. The optimal doping concentration of Mn $^{4+}$ ions in SLMS: x Mn $^{4+}$ phosphors was $x = 0.8\%$. It was worth noting that the emission intensity of the SLMS:0.8%Mn $^{4+}$ phosphors was remained about 55% at 363 K compared with that at 303 K, indicating that the as-prepared phosphors showed good thermal-stability behavior. Furthermore, the IQE of the SLMS:0.8%Mn $^{4+}$ phosphors reached as high as 35%. All the above results suggest that the SLMS: x Mn $^{4+}$ phosphors with far-red emission possess an outstanding potential to be used as far-red emitting phosphors in the application of far-red LEDs for indoor plant growth.

Conflicts of interest

There are no conflicts to declare.

Acknowledgements

This work was supported by the National Natural Science Foundation of China (No. 51502190), the Program for the Outstanding Innovative Teams of Higher Learning Institutions



of Shanxi, and the Open Fund of the State Key Laboratory of Luminescent Materials and Devices (South China University of Technology, No. 2017-skllmd-01).

References

- 1 J. Zhong, W. Zhao, L. Yang, P. Shi, Z. Liao, M. Xia, W. Pu, W. Xiao and L. Wang, *RSC Adv.*, 2018, **8**, 13054–13060.
- 2 F. Du, W. Zhuang, R. Liu, Y. Liu, J. Zhong, P. Gao, X. Zhang, W. Gao and L. Shao, *RSC Adv.*, 2017, **7**, 1075–1081.
- 3 X. Huang, *J. Alloys Compd.*, 2017, **690**, 356–359.
- 4 G.-G. Wang, X.-F. Wang, L.-W. Dong and Q. Yang, *RSC Adv.*, 2016, **6**, 42770–42777.
- 5 D. Qin and W. Tang, *RSC Adv.*, 2017, **7**, 2494–2502.
- 6 X. Huang, *Nat. Photonics*, 2014, **8**, 748–749.
- 7 P. Du, X. Huang and J. S. Yu, *Inorg. Chem. Front.*, 2017, **4**, 1987–1995.
- 8 P. Du, L. Luo, X. Huang and J. S. Yu, *J. Colloid Interface Sci.*, 2018, **514**, 172–181.
- 9 H. Guo, B. Devakumar, B. Li and X. Huang, *Dyes Pigm.*, 2018, **151**, 81–88.
- 10 Z. Zhou, J. Zheng, R. Shi, N. Zhang, J. Chen, R. Zhang, H. Suo, E. M. Goldys and C. Guo, *ACS Appl. Mater. Interfaces*, 2017, **9**, 6177–6185.
- 11 H. Smith, *Nature*, 2000, **407**, 585–591.
- 12 J. Chen, N. Zhang, C. Guo, F. Pan, X. Zhou, H. Suo, X. Zhao and E. M. Goldys, *ACS Appl. Mater. Interfaces*, 2016, **8**, 20856–20864.
- 13 Y. Zheng, H. Zhang, H. Zhang, Z. Xia, Y. Liu, M. S. Molokeev and B. Lei, *J. Mater. Chem. C*, 2018, **6**, 4217–4224.
- 14 L. Li, Y. Pan, Z. Chen, S. Huang and M. Wu, *RSC Adv.*, 2017, **7**, 14868–14875.
- 15 S. Wang, Q. Sun, B. Devakumar, L. Sun, J. Liang and X. Huang, *RSC Adv.*, 2018, **8**, 30191–30200.
- 16 Z. Zhou, Y. Zhong, M. Xia, N. Zhou, B. Lei, J. Wang and F. Wu, *J. Mater. Chem. C*, 2018, **6**, 8914–8922.
- 17 Y. Li, S. Qi, P. Li and Z. Wang, *RSC Adv.*, 2017, **7**, 38318–38334.
- 18 T. Senden, E. J. van Harten and A. Meijerink, *J. Lumin.*, 2018, **194**, 131–138.
- 19 L. Qin, S. Bi, P. Cai, C. Chen, J. Wang, S. I. Kim, Y. Huang and H. J. Seo, *J. Alloys Compd.*, 2018, **755**, 61–66.
- 20 T. T. Deng, E. H. Song, J. Su, Y. Y. Zhou, L. Y. Wang, S. Ye and Q. Y. Zhang, *J. Mater. Chem. C*, 2018, **6**, 4418–4426.
- 21 P. Cai, L. Qin, C. Chen, J. Wang, S. Bi, S. I. Kim, Y. Huang and H. J. Seo, *Inorg. Chem.*, 2018, **57**, 3073–3081.
- 22 L. Y. Wang, E. H. Song, T. T. Deng, Y. Y. Zhou, Z. F. Liao, W. R. Zhao, B. Zhou and Q. Y. Zhang, *Dalton Trans.*, 2017, **46**, 9925–9933.
- 23 T. Sasaki, J. Fukushima, Y. Hayashi and H. Takizawa, *J. Lumin.*, 2017, **188**, 101–106.
- 24 P. Cai, L. Qin, C. Chen, J. Wang and H. J. Seo, *Dalton Trans.*, 2017, **46**, 14331–14340.
- 25 M. Zhu, Y. Pan, Y. Huang, H. Lian and J. Lin, *J. Mater. Chem. C*, 2018, **6**, 491–499.
- 26 Z. Wang, N. Wang, Z. Yang, Z. Yang, Q. Wei, Q. Zhou and H. Liang, *J. Lumin.*, 2017, **192**, 690–694.
- 27 H. Ming, S. Liu, L. Liu, J. Peng, J. Fu, F. Du and X. Ye, *ACS Appl. Mater. Interfaces*, 2018, **10**, 19783–19795.
- 28 X. Huang and H. Guo, *Dyes Pigm.*, 2018, **152**, 36–42.
- 29 R. Cao, Z. Shi, G. Quan, T. Chen, S. Guo, Z. Hu and P. Liu, *J. Lumin.*, 2017, **188**, 577–581.
- 30 J. Zhong, S. Zhou, D. Chen, J. Li, Y. Zhu, X. Li, L. Chen and Z. Ji, *Dalton Trans.*, 2018, **47**, 8248.
- 31 J. Chen, C. Guo, Z. Yang, T. Li, J. Zhao and J. McKittrick, *J. Am. Ceram. Soc.*, 2016, **99**, 218–225.
- 32 K. Seki, K. Uematsu, K. Toda and M. Sato, *Chem. Lett.*, 2014, **43**, 1213–1215.
- 33 L. Ma, D.-j. Wang, Z.-y. Mao, Q.-f. Lu and Z.-h. Yuan, *Appl. Phys. Lett.*, 2008, **93**, 144101.
- 34 R. Cao, Z. Shi, G. Quan, Z. Luo, P. Tang, H. Ao and X. Yu, *Opt. Mater.*, 2016, **57**, 212–216.
- 35 X. Huang, J. Liang, B. Li, L. Sun and J. Lin, *Opt. Lett.*, 2018, **43**, 3305–3308.
- 36 Q. Sun, S. Wang, B. Devakumar, B. Li, L. Sun, J. Liang and X. Huang, *RSC Adv.*, 2018, **8**, 28538–28545.
- 37 J. Liang, L. Sun, B. Devakumar, S. Wang, Q. Sun, H. Guo, B. Li and X. Huang, *RSC Adv.*, 2018, **8**, 27144–27151.
- 38 Q. Liu, L. Wang, W. Huang, X. Li, M. Yu and Q. Zhang, *Ceram. Int.*, 2017, **43**, 16292–16299.
- 39 X. Zhang, J. Nie, S. Liu, Y. Li and J. Qiu, *J. Am. Ceram. Soc.*, 2018, **101**, 1576–1584.
- 40 Z. Lu, H. Wang, D. Yu, T. Huang, L. Wen, M. Huang, L. Zhou and Q. Wang, *Opt. Laser Technol.*, 2018, **108**, 116–123.
- 41 G. Jiang, B. Yang, G. Zhao, Y. Liu, J. Zou, H. Sun, H. Ou, Y. Fang and J. Hou, *Opt. Mater.*, 2018, **83**, 93–98.
- 42 X. Huang, H. Guo and B. Li, *J. Alloys Compd.*, 2017, **720**, 29–38.
- 43 X. Huang, B. Li and H. Guo, *J. Alloys Compd.*, 2017, **695**, 2773–2780.
- 44 K. Li, H. Lian and R. V. Deun, *J. Lumin.*, 2018, **198**, 155–162.
- 45 T. Jansen, J. Gorobez, M. Kirm, M. G. Brik, S. Vielhauer, M. Oja, N. M. Khaidukov, V. N. Makhov and T. Jüstel, *ECS J. Solid State Sci. Technol.*, 2018, **7**, R3086–R3092.
- 46 A. Fu, L. Zhou, S. Wang and Y. Li, *Dyes Pigm.*, 2018, **148**, 9–15.
- 47 U. B. Humayoun, S. N. Tiruneh and D.-H. Yoon, *Dyes Pigm.*, 2018, **152**, 127–130.
- 48 S. Zhang, Y. Hu, H. Duan, Y. Fu and M. He, *J. Alloys Compd.*, 2017, **693**, 315–325.
- 49 J. Long, Y. Wang, R. Ma, C. Ma, X. Yuan, Z. Wen, M. Du and Y. Cao, *Inorg. Chem.*, 2017, **56**, 3269–3275.
- 50 K. Li, D. Zhu and R. Van Deun, *Dyes Pigm.*, 2017, **142**, 69–76.
- 51 A. Fu, C. Zhou, Q. Chen, Z. Lu, T. Huang, H. Wang and L. Zhou, *Ceram. Int.*, 2017, **43**, 6353–6362.
- 52 K. Li, H. Lian and R. Van Deun, *Dalton Trans.*, 2018, **47**, 2501–2505.
- 53 Z. Lu, T. Huang, R. Deng, H. Wang, L. Wen, M. Huang, L. Zhou and C. Yao, *Superlattices Microstruct.*, 2018, **117**, 476–487.
- 54 R. Cao, X. Liu, K. Bai, T. Chen, S. Guo, Z. Hu, F. Xiao and Z. Luo, *J. Lumin.*, 2018, **197**, 169–174.
- 55 B. Li, X. Huang, H. Guo and Y. Zeng, *Dyes Pigm.*, 2018, **150**, 67–72.



- 56 H. Guo, X. Huang and Y. Zeng, *J. Alloys Compd.*, 2018, **741**, 300–306.
- 57 X. Huang, B. Li, H. Guo and D. Chen, *Dyes Pigm.*, 2017, **143**, 86–94.
- 58 Z. Zhou, M. Xia, Y. Zhong, S. Gai, S. Huang, Y. Tian, X. Lu and N. Zhou, *J. Mater. Chem. C*, 2017, **5**, 8201–8210.
- 59 J. Y. Park, J. S. Joo, H. K. Yang and M. Kwak, *J. Alloys Compd.*, 2017, **714**, 390–396.
- 60 J. Zhong, D. Chen, X. Chen, K. Wang, X. Li, Y. Zhu and Z. Ji, *Dalton Trans.*, 2018, **47**, 6528–6537.
- 61 J. Zhong, D. Chen, S. Yuan, M. Liu, Y. Yuan, Y. Zhu, X. Li and Z. Ji, *Inorg. Chem.*, 2018, **57**, 8978–8987.
- 62 D. Chen, Y. Zhou, W. Xu, J. Zhong, Z. Ji and W. Xiang, *J. Mater. Chem. C*, 2016, **4**, 1704–1712.
- 63 P. Du, X. Huang and J. S. Yu, *Chem. Eng. J.*, 2018, **337**, 91–100.
- 64 X. Huang, S. Wang, B. Li, Q. Sun and H. Guo, *Opt. Lett.*, 2018, **43**, 1307–1310.
- 65 C. Yang, Z. Zhang, G. Hu, R. Cao, X. Liang and W. Xiang, *J. Alloys Compd.*, 2017, **694**, 1201–1208.
- 66 Q. Peng, R. Cao, Y. Ye, S. Guo, Z. Hu, T. Chen and G. Zheng, *J. Alloys Compd.*, 2017, **725**, 139–144.
- 67 S. J. Kim, H. S. Jang, S. Unithrattil, Y. H. Kim and W. B. Im, *J. Lumin.*, 2016, **172**, 99–104.
- 68 R. Cao, Y. Ye, Q. Peng, G. Zheng, H. Ao, J. Fu, Y. Guo and B. Guo, *Dyes Pigm.*, 2017, **146**, 14–19.

